

# PolGS++: Physically-Guided Polarimetric Gaussian Splatting for Fast Reflective Surface Reconstruction

Yufei Han<sup>1</sup>, Chu Zhou<sup>2</sup>, Youwei Lyu<sup>3</sup>, Qi Chen<sup>1</sup>, Si Li<sup>1</sup>, Boxin Shi<sup>4,5</sup>, Yunpeng Jia<sup>1</sup>, Heng Guo<sup>1\*</sup>, Zhanyu Ma<sup>1</sup>

Received: date / Accepted: date

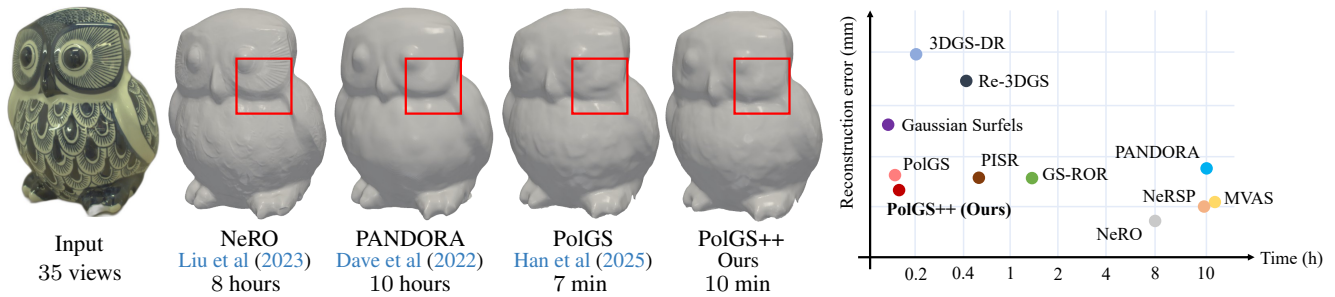


Fig. 1: Comparison of efficiency and accuracy on reflective surface reconstruction. Our method takes only 10 minutes while achieving a shape reconstruction accuracy (measured by Chamfer Distance in millimeters) comparable to that of the neural implicit surface representation-based method NeRO (Liu et al, 2023).

**Abstract** Accurate reconstruction of reflective surfaces remains a fundamental challenge in computer vision, with broad applications in real-time virtual reality and digital content creation. Although 3D Gaussian Splatting (3DGS) enables efficient novel-view rendering with explicit representations, its performance on reflective surfaces still lags behind implicit neural methods, especially in recovering fine geometry and surface normals. To address this gap, we propose PolGS++, a physically-guided polarimetric Gaussian Splatting framework for fast reflective surface reconstruction. Specifically, we integrate a polarized BRDF (pBRDF) model into 3DGS to explicitly decouple diffuse and specular components, providing physically grounded reflectance modeling and stronger geometric cues for reflective surface recovery. Furthermore, we introduce a *depth-guided visibility mask*

*acquisition* mechanism that enables angle-of-polarization (AoP)-based tangent-space consistency constraints in Gaussian Splatting without costly ray-tracing intersections. This physically guided design improves reconstruction quality and efficiency, requiring only about 10 minutes of training. Extensive experiments on both synthetic and real-world datasets validate the effectiveness of our method. Code page: [https://github.com/PRIS-CV/PolGS\\_plus](https://github.com/PRIS-CV/PolGS_plus).

**Keywords** Polarization-based vision; Reflective surface reconstruction; 3D Gaussian Splatting

## 1 Introduction

Accurate and robust reconstruction of reflective surfaces is essential for applications such as real-time virtual reality, digital content creation, and inverse rendering. Reflective materials remain challenging for 3D reconstruction because their view-dependent specular appearance violates the photometric consistency assumptions widely used by multi-view stereo and neural rendering methods. Therefore, jointly modeling light-surface interaction and geometric consistency with physically grounded constraints remain a fundamental open problem.

Corresponding author: Heng Guo

E-mail: guoheng@bupt.edu.cn

- 1 Beijing University of Posts and Telecommunications, China
- 2 National Institute of Informatics, Japan
- 3 vivo BlueImage Lab, vivo Mobile Communication Co., Ltd., Shanghai, China
- 4 State Key Laboratory for Multimedia Information Processing, School of Computer Science, Peking University, China
- 5 National Engineering Research Center of Visual Technology, School of Computer Science, Peking University, China

Most existing reflective-surface reconstruction methods are built on implicit neural representations (Mildenhall et al, 2020), such as Ref-NeRF (Verbin et al, 2022) and NeRO (Liu et al, 2023). These methods model view-dependent reflectance and typically recover geometry through an implicit Signed Distance Field (SDF). Polarization-based approaches further improve reconstruction quality by injecting physically grounded cues. Some methods (Dave et al, 2022; Han et al, 2024; Li et al, 2024b, 2025) leverage the polarimetric bidirectional reflectance distribution function (pBRDF) (Baek et al, 2018), while others (Zhao et al, 2022; Cao et al, 2023; Han et al, 2024; Chen et al, 2024b) exploit angle-of-polarization (AoP) observations to constrain surface normals and reduce geometric ambiguity. Nevertheless, these methods still rely heavily on implicit optimization with volumetric sampling and MLP-based fitting, leading to high computational overhead and slow reconstruction.

In contrast, 3D Gaussian Splatting (3DGS) (Kerbl et al, 2023) provides an explicit representation with highly efficient rendering. However, this efficiency does not directly translate to strong shape modeling, since 3DGS lacks direct supervision and structural regularization for surface normals. Consequently, geometric constraints remain weak and reconstructions are often unreliable; this limitation is more pronounced on reflective surfaces. Therefore, most 3DGS-based reconstruction methods mainly focus on diffuse scenes (Chen et al, 2023; Yu et al, 2024a; Lyu et al, 2024a; Guédon and Lepetit, 2024; Dai et al, 2024; Huang et al, 2024).

To address these issues, we propose **PolGS++**, a physically-guided polarimetric Gaussian Splatting framework for fast reflective surface reconstruction. By leveraging *photometric* cues from polarization, we build a pBRDF model in explicit 3DGS to decouple diffuse and specular components, providing physically grounded supervision for reflective appearance and shape recovery. To realize this design, we adopt an enhanced 3DGS representation (Gaussian Surfels (Dai et al, 2024)) as the geometric backbone and incorporate a Cubemap Encoder inspired by 3DGS-DR (Ye et al, 2024) to model specular reflections. This pBRDF-guided decomposition retains the efficiency of explicit Gaussian rendering while improving reflective shape reconstruction.

Beyond photometric cues, we also aim to exploit *geometric* cues from polarization to further improve reconstruction quality. A natural choice is the multi-view tangent-space consistency (TSC) loss (Cao et al, 2023; Han et al, 2024). However, the existing TSC constrain is developed for implicit surface representations and relies on explicit ray-surface intersections to determine cross-view visibility masks, which is highly time-consuming. Due to splatting-based rasterization, this formulation cannot be directly applied to 3DGS.

To enable TSC in the Gaussian Splatting pipeline, we design a *depth-guided visibility mask acquisition* mechanism that avoids ray-tracing during optimization. Specifically, we

Table 1: Comparison of different methods in reflective surface reconstruction on real-world datasets (Dave et al, 2022; Chen et al, 2024b; Han et al, 2024) with the image size  $512 * 612$ .

Method	Input	Reflective	Type	Accuracy	Time
NeRO (Liu et al, 2023)	RGB Images	✓	SDF	high	8h
MVAS (Cao et al, 2023)	Azimuths	✓	SDF	medium	11h
PANDORA (Dave et al, 2022)	Pol. Images	✓	SDF	medium	10h
NeRSP (Han et al, 2024)	Pol. Images	✓	SDF	high	10h
PISR (Chen et al, 2024b)	Pol. Images	✓	SDF	medium	0.5h
GS-ROR (Zhu et al, 2025)	RGB Images	✓	SDF+GS	medium	1.5h
Gaussian Surfels (Dai et al, 2024)	RGB Images	✗	GS	low	5m
3DGS-DR (Ye et al, 2024)	RGB Images	✓	GS	low	12m
Re-3DGS (Gao et al, 2024)	RGB Images	✓	GS	low	25m
PolGS++ (Ours)	Pol. Images	✓	GS	medium	10m

estimate visibility by comparing rendered depth maps with the point-to-camera distances of candidate surface points. This design enables, for the first time, the integration of multi-view tangent-space constraints into a 3DGS-based reconstruction framework, bridging the gap between implicit SDF-based methods and explicit Gaussian representations.

With these polarimetric constraints, PolGS++ resolves shape ambiguities that cannot be handled by RGB-only supervision and accurately reconstructs *reflective* and *texture-less* objects within 10 minutes. As shown in Fig. 1 and Table 1, PolGS++ achieves reconstruction quality comparable to state-of-the-art SDF-based methods while maintaining over  $80\times$  speedup, making it suitable for real-time and large-scale reflective surface reconstruction.

In summary, we advance the reflective surface reconstruction by proposing:

- PolGS++, a physically-guided polarimetric 3D Gaussian Splatting framework for fast reflective surface reconstruction.
- A pBRDF module in 3DGS that constrains both diffuse and specular components of reflective surfaces.
- A depth-guided visibility mask acquisition mechanism that enables multi-view tangent-space consistency loss in the 3DGS framework without ray-surface intersection.

The preliminary version of this work, PolGS (Han et al, 2025), considered only pBRDF integration with 3DGS and did not fully exploit polarimetric cues. This journal article extends PolGS (Han et al, 2025) by introducing a multi-view TSC constraint in 3DGS architecture and enabling it through the proposed depth-guided visibility mask acquisition strategy. This extension resolves azimuth ambiguity in monocular polarimetric cues and enforces stronger cross-view geometric consistency. Specifically, in Sec. 4.2, we provide a detailed analysis of the depth-guided visibility mask acquisition mechanism. In Sec. 5, we present more comprehensive evaluations, including expanded ablations on polarimetric information and the threshold used in the depth-guided visibility mask. We also provide broader validation on synthetic and real-world datasets, demonstrating improved robustness and reconstruction quality.

## 2 Related work

Our method aims to reconstruct reflective surfaces via 3DGS using polarized images, so we summarize recent progresses in 3D reconstruction techniques, focusing on reflective surfaces through SDF-based methods, 3DGS methods, and polarized image-based reconstruction, respectively.

### 3D reconstruction based on neural SDF representation

Novel view synthesis has achieved great success using Neural Radiance Fields (NeRF (Mildenhall et al, 2020)). Motivated by the structure of the multi-layer perceptron (MLP) network within NeRFs, numerous 3D reconstruction methods have emerged that leverage implicit neural representations to predict object surfaces. Some approaches (Niemeyer et al, 2020; Yariv et al, 2020) proposed the signed distance field (SDF) into the neural radiance field, effectively representing the surface as an implicit function. Other works (Wang et al, 2021; Yariv et al, 2021; Oechsle et al, 2021; Wang et al, 2022, 2023; Li et al, 2023b) extend it by proposing efficient framework in detailed surface reconstruction.

These methods based on SDF represent complex scenes implicitly, but they typically suffer from high computational demands and are not suitable for real-time applications. Although some methods (Wang et al, 2023; Li et al, 2023b) utilize hash grids and instant-NGP (Müller et al, 2022) structure, it is still a challenge for them to reconstruct the mesh efficiently facing the reflective surface.

Ref-NeRF (Verbin et al, 2022) uses the Integrated Directional Encoding (IDE) structure to estimate the specular reflection components of the object surface by using predicted roughness, view direction, and surface normals. NeRO (Liu et al, 2023) improves it by generating the physically-based rendering (PBR) parameters, and NeP (Wang et al, 2024) can better deal with the glossy surface. TensoSDF (Li et al, 2024c) combines a novel tensorial representation (Chen et al, 2022) with the radiance and reflectance field for robust geometry reconstruction. Overall, these approaches cannot avoid long optimization times, which limit their practicality for reflective scenes.

**3D reconstruction based on 3DGS** 3DGS (Kerbl et al, 2023) aims to address limitations of neural radiance fields by representing complex spatial points using 3D Gaussian ellipsoids. However, 3D Gaussian ellipsoids often fail to conform closely to true object surfaces, leading to inaccurate geometry and degraded point-cloud quality.

To overcome these drawbacks, several extensions and modifications have been proposed. SuGaR (Guédon and Lepetit, 2024) approximates 2D Gaussians with 3D Gaussians, NeuSG (Chen et al, 2023), GSDF (Yu et al, 2024a) and 3DGSR (Lyu et al, 2024a) integrate an extra SDF network for representing surface normals to supervise the Gaussian Splatting geometry. 2D Gaussian Splatting (Huang et al, 2024)

and Gaussian Surfels (Dai et al, 2024) have taken a different approach by transforming the 3D ellipsoids into 2D ellipses for modeling. This transformation allows for more refined constraints on depth and normal consistency, addressing the surface approximation issues more effectively. GOF (Yu et al, 2024b) achieves more realistic mesh generation through its innovative opacity rendering strategy. PGSR (Chen et al, 2024a) utilizes single-view and multi-view regularization on planar Gaussians to achieve high-precision global geometric consistency. However, these methods do not focus on reflective surface reconstruction.

Re-3DGS (Gao et al, 2024) associates extra properties, including normal vectors, BRDF parameters, and incident lighting from various directions to make photo-realistic re-lighting. 3DGS-DR (Ye et al, 2024) presents a deferred shading method to effectively render specular reflection with Gaussian splatting. GS-ROR (Zhu et al, 2025) integrates the SDF-based representation into 3DGS to improve surface modeling, but it still relies on a costly SDF optimization stage. Despite these advancements, these methods still face challenges in many scenarios and cannot provide accurate geometric representations.

**3D reconstruction using polarized images** Polarized images are widely used in Shape from Polarization (SfP) (Miyazaki et al, 2003; Baek et al, 2018; Smith et al, 2018; Deschaintre et al, 2021; Lei et al, 2022; Ba et al, 2020; Lyu et al, 2023; Li et al, 2024a; Yang et al, 2024; Lyu et al, 2024b), reflection removal (Li et al, 2020; Lyu et al, 2022; Wang et al, 2025), and some downstream tasks (Zhou et al, 2023; Li et al, 2023a) due to the strong physics-preliminary information in the Stokes field. The SfP task aims to predict the surface normal captured by the polarization camera under the single distant light (Lyu et al, 2023; Smith et al, 2018) or unknown ambient light (Ba et al, 2020; Lei et al, 2022). Multi-view 3D reconstruction works using polarized images (Zhao et al, 2022) try to settle down the  $\pi$  and  $\pi/2$  ambiguities with the Angle of Polarization (AoP). PANDORA (Dave et al, 2022) first uses polarized images in neural 3D reconstruction work, following the relevant constraints of pBRDF (Baek et al, 2018). MVAS (Cao et al, 2023) leverages multi-view AoP maps to generate tangent spaces for surface points during the optimization process, which can reconstruct mesh without rendering supervision. NeRSP (Han et al, 2024) combines the photometric and geometric cues from polarized images and generates better results under sparse views for reflective surfaces. PISR (Chen et al, 2024b) focuses on textureless specular surface and integrates the multi-resolution hash grid for efficiency. NeISF (Li et al, 2024b) considers inter-reflection and models multi-bounce polarized light paths during rendering. Furthermore, NeISF++ (Li et al, 2025) extends this approach to conductive surfaces. Despite these advancements, computational cost remains a significant limitation for many polarized-based 3D reconstruction methods.

### 3 Preliminaries

#### 3.1 Gaussian Surfels model

Our method adopts Gaussian Surfels (Dai et al, 2024) as the base framework, leveraging its superior geometric representation capabilities. Following Gaussian Surfels (Dai et al, 2024), we use a set of unstructured Gaussian kernels  $\{G_i = \{\mathbf{x}_i, \mathbf{s}_i, \mathbf{r}_i, o_i, C_i\} | i \in \mathcal{N}\}$  to represent the structure of 3DGS, where  $\mathbf{x}_i \in \mathbb{R}^3$  denotes the center position of each Gaussian kernel,  $\mathbf{s}_i = [s_i^x, s_i^y, 0]^\top \in \mathbb{R}^3$  is the scaling factors of  $x$  and  $y$  axes after flattening the 3D Gaussians (Kerbl et al, 2023),  $\mathbf{r}_i \in \mathbb{R}^4$  is the rotation quaternion,  $o_i \in \mathbb{R}$  is the opacity, and  $C_i \in \mathbb{R}^k$  represents the spherical harmonic coefficients of each Gaussian. The Gaussian distribution can be defined by the covariance matrix  $\Sigma$  of a 3D Gaussian as:

$$G(\mathbf{x}; \mathbf{x}_i, \Sigma_i) = \exp\left(-\frac{1}{2}(\mathbf{x} - \mathbf{x}_i)^\top \Sigma_i^{-1}(\mathbf{x} - \mathbf{x}_i)\right), \quad (1)$$

where  $\Sigma_i$  can be represented as:

$$\begin{aligned} \Sigma_i &= \mathbf{R}(\mathbf{r}_i) \mathbf{s}_i \mathbf{s}_i^\top \mathbf{R}(\mathbf{r}_i)^\top \\ &= \mathbf{R}(\mathbf{r}_i) \text{Diag}[(s_i^x)^2, (s_i^y)^2, 0] \mathbf{R}(\mathbf{r}_i)^\top, \end{aligned} \quad (2)$$

where  $\text{Diag}[\cdot]$  indicates a diagonal matrix and  $\mathbf{R}(\mathbf{r}_i)$  is a  $3 \times 3$  rotation matrix represented by  $\mathbf{r}_i$ .

**Gaussian splatting** The novel view rendering process can be represented as (Kerbl et al, 2023):

$$C = \sum_{i=0}^n T_i \alpha_i c_i, \quad (3)$$

where  $T_i = \prod_{j=0}^{i-1} (1 - \alpha_j)$  is the transmittance,  $\alpha_i = G'(\mathbf{u}; \mathbf{u}_i, \Sigma'_i) o_i$  is alpha-blending weight, which is the product of opacity and the Gaussian weight based on pixel  $\mathbf{u}$ . In order to speed up the rendering process, the 3D Gaussian in Eq. (2) is re-parameterized in 2D ray space (Zwicker et al, 2002) as  $G'$ :

$$G'(\mathbf{u}; \mathbf{u}_i, \Sigma'_i) = \exp\left(-\frac{1}{2}(\mathbf{u} - \mathbf{u}_i)^\top \Sigma'_i{}^{-1}(\mathbf{u} - \mathbf{u}_i)\right), \quad (4)$$

where  $\Sigma'_i = (\mathbf{J}_k \mathbf{W}_k \Sigma_i \mathbf{W}_k^\top \mathbf{J}_k^\top)[2, : 2]$  represents the covariance matrix in the 2D ray space. The  $\mathbf{W}_k$  is a viewing transformation matrix for input image  $k$  and  $\mathbf{J}_k$  is the affine approximation of the projective transformation.

The depth  $\tilde{D}$  and normal  $\tilde{N}$  for each pixel can also be calculated via Gaussian splatting and alpha-blending (Dai et al, 2024):

$$\tilde{D} = \frac{1}{1 - T_{n+1}} \sum_{i=0}^n T_i \alpha_i d_i(\mathbf{u}), \quad (5)$$

$$\tilde{N} = \frac{1}{1 - T_{n+1}} \sum_{i=0}^n T_i \alpha_i \mathbf{R}_i[:, 2]. \quad (6)$$

Specifically, according to Gaussian Surfels (Dai et al, 2024), the depth of pixel  $\mathbf{u}$  for each Gaussian kernel  $i$  is computed by calculating the intersection of the ray cast through pixel  $\mathbf{u}$  with the Gaussian ellipse during splatting. So  $d_i(\mathbf{u})$  can be represented by Taylor expansion as:

$$d_i(\mathbf{u}) = d_i(\mathbf{u}_i) + (\mathbf{W}_k \mathbf{R}_i)[2, :] \mathbf{J}_{pr}^{-1}(\mathbf{u} - \mathbf{u}_i), \quad (7)$$

where  $\mathbf{J}_{pr}^{-1}$  is the Jacobian inverse mapping one pixel from image space to tangent plane of the Gaussian surfel (Zwicker et al, 2001), and  $(\mathbf{W}_k \mathbf{R}_i)$  transforms the rotation matrix of a Gaussian surfel to the camera space.

#### 3.2 Polarimetric image formation model

Polarization cameras can capture polarized images in a single shot, which can be represented as four different polarized angles of images  $I = [I_0, I_{45}, I_{90}, I_{135}]$ . The Stokes vector  $\mathbf{s} = \{s_0, s_1, s_2, s_3\}$  can be calculated by:

$$\mathbf{s} = \begin{bmatrix} \frac{1}{2}(I_0 + I_{45} + I_{90} + I_{135}) \\ I_0 - I_{90} \\ I_{45} - I_{135} \\ 0 \end{bmatrix}, \quad (8)$$

where we assume the light source is not circularly polarized following prior works (Dave et al, 2022; Han et al, 2024), thus the  $s_3$  is 0. The Stokes vector can be used to compute the angle of polarization (AoP), *i.e.*

$$\varphi = \frac{1}{2} \arctan\left(\frac{s_2}{s_1}\right). \quad (9)$$

According to PANDORA (Dave et al, 2022) and NeRSP (Han et al, 2024), we assume the incident environmental illumination is unpolarized, and the Stokes vector for the incident light direction  $\boldsymbol{\omega}$  can be expressed as:

$$\mathbf{s}_i(\boldsymbol{\omega}) = L(\boldsymbol{\omega})[1, 0, 0, 0]^\top, \quad (10)$$

where  $L(\boldsymbol{\omega})$  represents the light intensity. The polarization camera captures outgoing light that becomes partially polarized due to reflection, which is modeled using a  $4 \times 4$  Muller matrix  $\mathbf{H}$ . The outgoing Stokes vector  $\mathbf{s}$  then is formulated as the integral of the incident Stokes vector multiplied by this Mueller matrix:

$$\mathbf{s}(\mathbf{v}) = \int_{\Omega} \mathbf{H} \mathbf{s}_i(\boldsymbol{\omega}) d\boldsymbol{\omega}, \quad (11)$$

where  $\mathbf{v}$  indicates the view direction and  $\Omega$  is the integral domain. Following the polarized BRDF (pBRDF) model proposed by Baek et al (2018), the output Stokes vector can be divided into diffuse and specular components, represented by  $\mathbf{H}_d$  and  $\mathbf{H}_s$  respectively.  $\mathbf{s}$  can be represented as:

$$\mathbf{s}(\mathbf{v}) = \int_{\Omega} \mathbf{H}_d \mathbf{s}_i(\boldsymbol{\omega}) d\boldsymbol{\omega} + \int_{\Omega} \mathbf{H}_s \mathbf{s}_i(\boldsymbol{\omega}) d\boldsymbol{\omega}. \quad (12)$$

Based on the derivations from PANDORA (Dave et al, 2022) and NeRSP (Han et al, 2024), The output Stokes vector can be further specified as:

$$\mathbf{s}(\mathbf{v}) = L_d \begin{bmatrix} T_o^+ \\ T_o^- \cos(2\phi_n) \\ -T_o^- \sin(2\phi_n) \\ 0 \end{bmatrix} + L_s \begin{bmatrix} R^+ \\ R^- \cos(2\phi_h) \\ -R^- \sin(2\phi_h) \\ 0 \end{bmatrix}, \quad (13)$$

where  $L_d = \int_{\Omega} \rho L(\omega) \omega^\top \mathbf{n} T_i^+ T_i^- d\omega$  denotes the diffuse radiance associated with the surface normal  $\mathbf{n}$ , Fresnel transmission coefficients (Baek et al, 2018)  $T_{i,o}^+$  and  $T_{i,o}^-$ . The diffuse albedo is represented by  $\rho$ , and  $\phi_n$  is the azimuth angle of the incident light.

Similarly,  $L_s = \int_{\Omega} L(\omega) \frac{DG}{4\mathbf{n}^\top \mathbf{v}} d\omega$  denotes the specular radiance, which involves Fresnel reflection coefficients (Baek et al, 2018)  $R^+$  and  $R^-$ , and the incident azimuth angle  $\phi_h$  concerning the half vector  $\mathbf{h} = \frac{\omega + \mathbf{v}}{\|\omega + \mathbf{v}\|_2}$ . For the sake of simplification in our model, we assume that  $\phi_h$  is equivalent to  $\phi_n$ . The Microfacet model incorporates the normal distribution and shadowing terms represented by  $D$  and  $G$  (Walter et al, 2007).

### 3.3 Multi-view tangent space consistency with AoP

Given AoP  $\varphi$  (as mentioned in Sec. 3.2), the azimuth angle of the surface can be either  $\varphi + \pi/2$  or  $\varphi + \pi$ , known as the  $\pi$  and  $\pi/2$  ambiguity, where  $\pi/2$  ambiguity depending on whether the surface is specular or diffuse dominant.

Following MVAS (Cao et al, 2023), for a scene point  $\mathbf{x}$ , its surface normal  $\mathbf{n}$  and the projected azimuth angle  $\phi$  in one camera view follow the relationship as

$$\mathbf{r}_1^\top \mathbf{n} \cos \phi - \mathbf{r}_2^\top \mathbf{n} \sin \phi = 0, \quad (14)$$

where  $\mathbf{R} = [\mathbf{r}_1, \mathbf{r}_2, \mathbf{r}_3]^\top$  is the rotation matrix of the camera pose. We can further re-arrange Eq. (14) to get the orthogonal relationship between surface normal and a projected tangent vector  $\mathbf{t}(\phi)$  as defined below,

$$\mathbf{n}^\top \underbrace{(\cos \phi \mathbf{r}_1 - \sin \phi \mathbf{r}_2)}_{\mathbf{t}(\phi)} = 0. \quad (15)$$

The  $\pi$  ambiguity between AoP and azimuth angle can be naturally resolved as Eq. (15) stands if we add  $\phi$  by  $\pi$ . The  $\pi/2$  ambiguity can be addressed by using a pseudo projected tangent vector  $\hat{\mathbf{t}}(\phi)$  such that

$$\mathbf{n}^\top \underbrace{(\sin \phi \mathbf{r}_1 + \cos \phi \mathbf{r}_2)}_{\hat{\mathbf{t}}(\phi)} = 0. \quad (16)$$

If one scene point  $\mathbf{x}$  is observed by  $k$  views, we can stack Eq. (15) and Eq. (16) based on  $k$  different rotations and observed AoPs, leading to a linear system

$$\mathbf{T}(\mathbf{x})\mathbf{n}(\mathbf{x}) = \mathbf{0}. \quad (17)$$

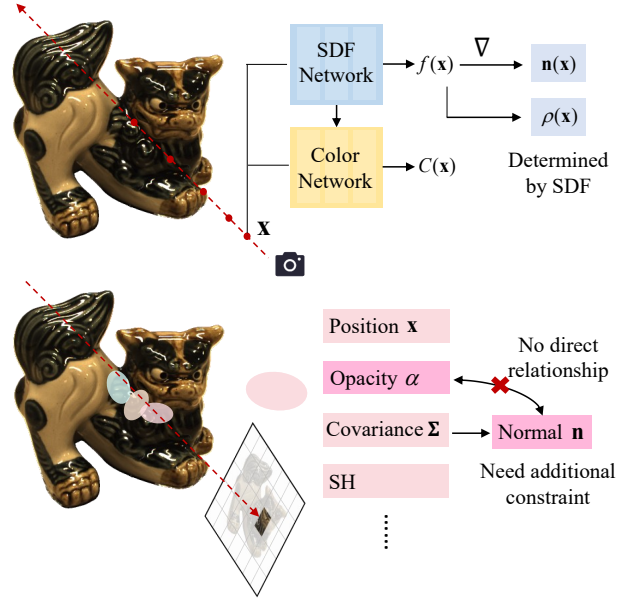


Fig. 2: Comparison between SDF-based and 3DGS-based method on geometry representation. **(Top)** The surface normal of a point has a strong relationship with its opacity in NeuS (Wang et al, 2021). **(Bottom)** The surface normal of a point has no direct dependence on its opacity in Gaussian Surfels (Dai et al, 2024).

In MVAS (Cao et al, 2023) and NeRSP (Han et al, 2024), the above linear system is used to formulate a multi-view tangent space consistency loss to constrain the surface normal estimation in neural implicit representations. However, directly applying such constraints in Gaussian Splatting frameworks remains challenging due to the lack of an explicit visibility definition across views. In Sec. 4.2, we propose a depth-guided visibility mask acquisition mechanism to address it.

## 4 Proposed method

The PolGS++ framework integrates multi-view polarized images, their corresponding masks, and camera pose information to produce a rich output that includes diffuse and specular components represented as Stokes vectors across various views, a reconstructed geometric mesh, and estimated environment light. In this section, we will analyze the surface normal representations employed in SDF-based approaches and 3DGS methods. Then we introduce a theoretical foundation for our polarization-guided reconstruction pipeline by using the polarimetric image formation model and multi-view tangent space consistency constraint.

### 4.1 Analysis of surface normal representation

In implicit neural networks, researchers employ signed distance functions (SDFs) to define surface boundaries, where

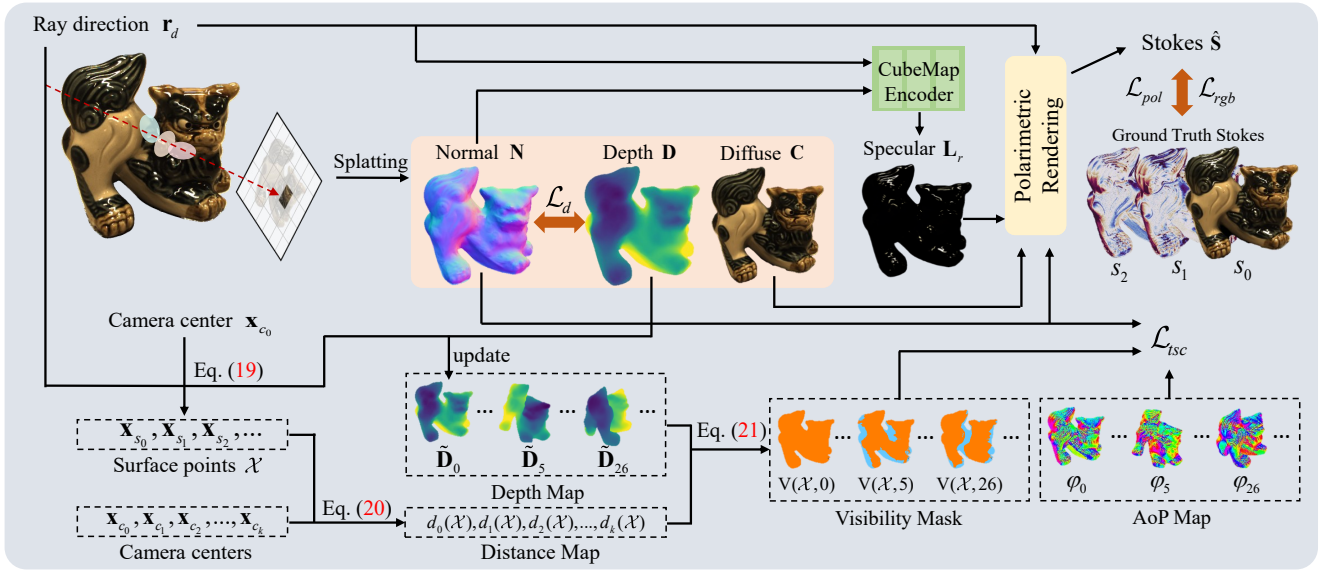


Fig. 3: Pipeline of PolGS++. We re-rendered Stokes vectors  $\hat{s}$  by using the diffuse color  $C$  from 3DGS and specular color  $L_r$  from Cubemap encoder module, which is supervised by the ground truth Stokes information. Tangent-space consistency constrain is applied to the surface normal estimated by 3DGS with the depth-guided visibility mask and AoP information.

surface normals are derived from the gradients of SDF. However, 3DGS methods often treat the surface normal as inherent properties typically. In this section, we provide a comparative analysis of surface normal representations in SDF-based methods versus 3DGS, explaining the reason we use polarimetric cues in the Gaussian Splatting method.

**SDF-based representation** The implicit neural network approach, exemplified by NeuS (Wang et al, 2021), enhances the constraints on the reconstructed surface by incorporating a Signed Distance Function (SDF). As illustrated at the top of Fig. 2, the SDF value  $f(\mathbf{x})$ , generated by the SDF Network, can be used to compute the normal vector  $\mathbf{n}(\mathbf{x})$  at point  $\mathbf{x}$ . According to the definition in (Wang et al, 2021), the opacity  $\rho(\mathbf{x})$  is given by:

$$\rho(\mathbf{x}) = \max\left(\frac{-\frac{d\Phi_s}{dx}(f(\mathbf{x}))}{\Phi_s(f(\mathbf{x}))}, 0\right), \quad (18)$$

where  $\Phi_s$  is a sigmoid function.

During optimization, the surface normal and the opacity at a given point influence each other. Consequently, after optimization, points farther from the surface tend to have lower opacity values, while the final normal vector is predominantly determined by points located on the surface. This mutual interaction results in a more precise and accurate representation of the surface.

**3DGS-based representation** In the case of Gaussian Surfels (Dai et al, 2024), surface normal is derived from the vector perpendicular to the plane of a 2D ellipsoid. As shown at the bottom of Fig. 2, for a single Gaussian kernel, there is no inherent relationship between opacity and the surface normal.

The pixel-level constraint in 3DGS creates a probabilistic representation where no single Gaussian kernel is definitively assigned to a surface. Consequently, multiple Gaussian kernel configurations can potentially represent equivalent surface geometries, introducing inherent reconstruction ambiguity. The optimization mechanism effectively blends contributions from multiple Gaussian points, which offers reconstruction adaptability but compromises the precision of individual point geometric characterizations.

It is obvious that using the normal prediction model (Eftekhari et al, 2021) as a prior constraint in Gaussian Splatting benefits object reconstruction, as demonstrated by Gaussian Surfels (Dai et al, 2024). However, the normal prediction model is not always reliable especially in reflective cases, highlighting the need for a more robust method to provide prior information.

**Polarimetric information for reflective surfaces** Reflective surface reconstruction is challenging due to the view-dependent appearance. Unlike traditional RGB image inputs, polarimetric information can effectively constrain the surface normal during the rendering of Stokes Vectors with the pBDRF model (Baek et al, 2018) and multi-view tangent space consistency constrain. Leveraging this property, we incorporate polarimetric information as a prior in shape reconstruction and use the 3DGS-based method to accelerate this process.

## 4.2 Pipeline of PolGS++

**Network structure** The network structure of PolGS++ is shown in Fig. 3. The framework comprises two primary com-

ponents: the Gaussian Surfels module and the CubeMap Encoder module. Initially, the Gaussian Surfels module is employed to estimate the diffuse component of the object, similar to the original Gaussian Surfels framework. Subsequently, we utilize the CubeMap Encoder to assess the specular component, akin to the approach taken in 3DGS-DR (Ye et al., 2024). While the CubeMap Encoder does not provide the roughness component, it effectively handles reflective or rough surfaces and maintains high computational efficiency due to its CUDA-based implementation.

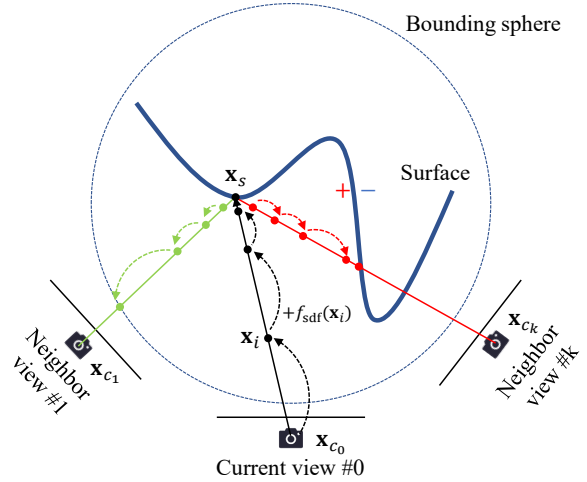
To enhance the rendering process, we incorporate a pBRDF model into the rendering formulation. This addition introduces a polarimetric constraint that further refines the Gaussian Splatting method, enabling more accurate and realistic 3D reconstructions. The final rendering formulation model following Eq. (13) can be represented as:

$$\hat{\mathbf{s}} = \begin{bmatrix} \hat{s}_0 \\ \hat{s}_1 \\ \hat{s}_2 \\ 0 \end{bmatrix} = C \begin{bmatrix} T_o^+ \\ T_o^- \cos(2\phi_n) \\ -T_o^- \sin(2\phi_n) \\ 0 \end{bmatrix} + L_r \begin{bmatrix} R^+ \\ R^- \cos(2\phi_h) \\ -R^- \sin(2\phi_h) \\ 0 \end{bmatrix}, \quad (19)$$

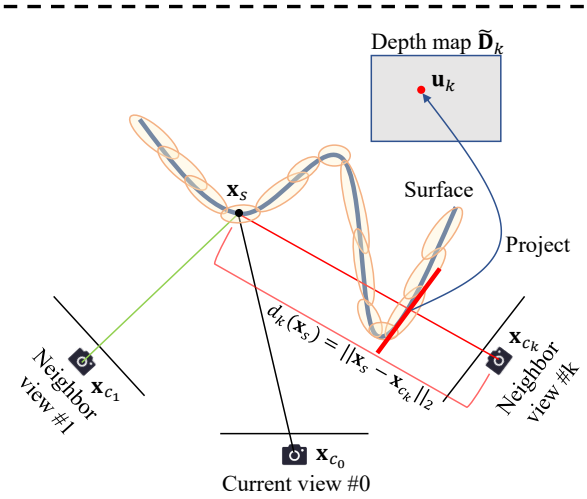
where  $C$  is the diffuse color after Gaussian Surfels rendering according to Eq. (3) and  $L_r$  is the specular color after CubeMap rendering  $E(\cdot)$ , which can be represented as  $L_r = E(\mathbf{r}_d - 2(\mathbf{r}_d \cdot \mathbf{n})\mathbf{n})$ .

**Depth-guided visibility mask** In addition to the polarimetric rendering, PolGS++ employs multi-view tangent space consistency to constrain surface geometry (Cao et al., 2023; Han et al., 2024). However, a key prerequisite is a reliable visibility mask to indicate whether a surface point is observable from a neighboring view. In implicit SDF-based representations, visibility can be classically evaluated via ray-tracing with the signed distance field (SDF). As shown in Fig. 4 (a), a surface point  $\mathbf{x}_s$  can be confirmed along the ray originating at camera center  $\mathbf{x}_{c_0}$  with direction  $r_d$  by iteratively stepping the ray by the SDF value until the first zero-crossing. To determine the visibility of  $\mathbf{x}_s$  from another view with camera center  $\mathbf{x}_{c_k}$ , one traces the ray from  $\mathbf{x}_s$  to  $\mathbf{x}_{c_k}$  and checks whether any surface intersection occurs before exiting the bounding sphere. If no intersection is detected, the visibility mask from view  $k$  is set as  $\mathbf{V}(\mathbf{x}_s, k) = 1$ ; otherwise,  $\mathbf{V}(\mathbf{x}_s, k) = 0$ .

However, this strategy is not directly applicable to Gaussian Splatting frameworks because they lack an explicit ray-surface intersection test. In 3DGS-based methods, the surface is represented by a set of Gaussian surfels and rendered via splatting and alpha compositing, making it non-trivial to backtrace whether a surface point is visible from another view. To address this limitation, we propose a *depth-guided visibility mask* acquisition strategy that leverages the depth maps produced during Gaussian Splatting.



(a) Visibility mask acquisition by ray-tracing in SDF-based methods.



(b) Depth-guided visibility mask acquisition in Gaussian Splatting.

Fig. 4: Comparison of visibility mask acquisition strategies between SDF-based methods and our method based on Gaussian Splatting.

As shown in Fig. 4 (b), we construct a set of pseudo-surface points  $\mathcal{X} = \{\mathbf{x}_s \in \mathbb{R}^3\}$  by back-projecting the rendered depth map of the reference view 0:

$$\mathbf{x}_s(\mathbf{u}) = \mathbf{x}_{c_0} + \tilde{\mathbf{D}}_0(\mathbf{u}) \mathbf{r}_0(\mathbf{u}), \quad (20)$$

where  $\mathbf{x}_{c_0}$  is the camera center of the reference view,  $\tilde{\mathbf{D}}_0$  denotes the rendered depth map,  $\mathbf{u}$  is the pixel coordinate, and  $\mathbf{r}_0(\mathbf{u})$  is the corresponding unit ray direction in world coordinates.

For a neighboring view  $k$  with camera center  $\mathbf{x}_{c_k}$ , we define the geometric distance from the camera to  $\mathbf{x}_s$  as

$$d_k(\mathbf{x}_s) = \|\mathbf{x}_s - \mathbf{x}_{c_k}\|_2. \quad (21)$$

Meanwhile, PolGS++ renders a depth map  $\tilde{\mathbf{D}}_k$  for view  $k$  at each splatting iteration. We cache  $\tilde{\mathbf{D}}_k$  in an auxiliary buffer

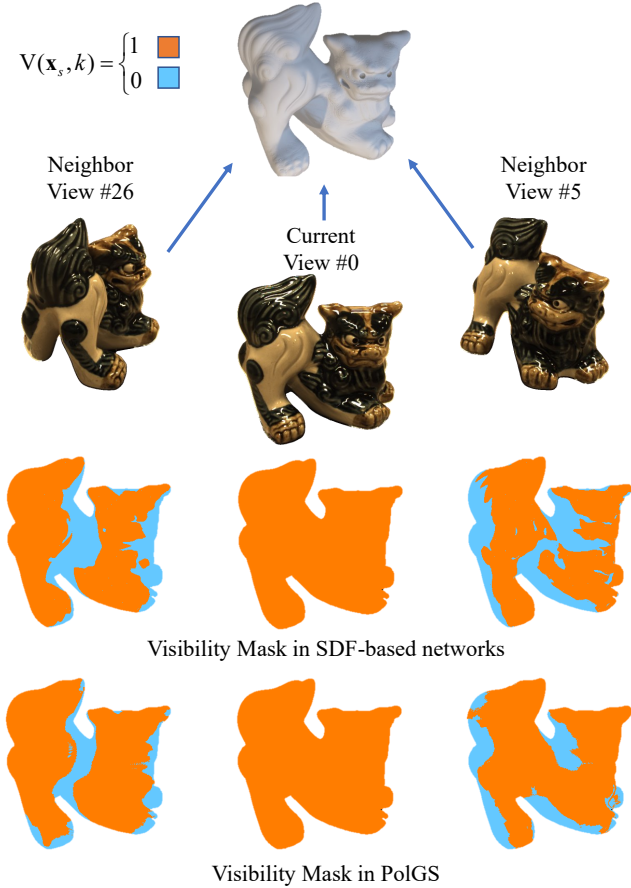


Fig. 5: Visualization of visibility masks of one current view in SDF-based networks and in PolGS++.

and detach it from backpropagation. By projecting  $\mathbf{x}_s$  onto the image plane of view  $k$ , we obtain the corresponding pixel coordinate  $\mathbf{u}_k = \pi_k(\mathbf{x}_s)$  and query the rendered depth value  $\tilde{\mathbf{D}}_k(\mathbf{u}_k)$ .

Ideally, if  $\mathbf{x}_s$  is visible from view  $k$ , the rendered depth along the viewing ray should agree with the geometric distance  $d_k(\mathbf{x}_s)$ . Therefore, we define the visibility mask as

$$\mathbf{V}(\mathbf{x}_s, k) = \begin{cases} 1, & |\tilde{\mathbf{D}}_k(\pi_k(\mathbf{x}_s)) - d_k(\mathbf{x}_s)| < \tau, \\ 0, & \text{otherwise,} \end{cases} \quad (22)$$

where  $\tau$  is a tolerance threshold that accounts for depth uncertainty caused by Gaussian blending and discretization effects.

Figure 5 compares visibility masks of SDF-based networks and PolGS++ from one current view. In SDF-based methods, we use ground-truth normals to supervise and obtain the visibility mask. Our depth-guided visibility mask estimation yields comparable results without explicit ray-tracing. Building upon this, we can formulate our multi-view tangent-space consistency constraint directly corresponding

to the defined linear system. Details of the ablation study about the visibility mask will be discussed in Sec. 5.3.

### 4.3 Training

The overall training loss in PolGS++ formulated as a comprehensive weighted sum of multiple loss components:

$$\mathcal{L} = \mathcal{L}_{rgb} + \lambda_1 \mathcal{L}_{pol} + \lambda_2 \mathcal{L}_{tsc} + \lambda_3 \mathcal{L}_m + \lambda_4 \mathcal{L}_o + \lambda_5 \mathcal{L}_d, \quad (23)$$

where we set  $\lambda_1 = 1$ ,  $\lambda_2 = 0.1$ ,  $\lambda_3 = 0.1$ ,  $\lambda_4 = 0.01$ ,  $\lambda_5 = 0.01 + 0.1 \cdot (\text{iteration}/15000)$  to balance the loss function.

**Rendering Stokes loss  $\mathcal{L}_{rgb}$  and  $\mathcal{L}_{pol}$**  The rendering Stokes loss is combined with the  $s_0$  (unpolarized image) rendering loss as 3DGS (Kerbl et al, 2023) and the  $s_1, s_2$  rendering loss as PANDORA (Dave et al, 2022). These two loss functions can be represented as:

$$\mathcal{L}_{rgb} = 0.8 \cdot L_1(s_0, \hat{s}_0) + 0.2 \cdot L_{D-SSIM}(s_0, \hat{s}_0), \quad (24)$$

$$\mathcal{L}_{pol} = L_1(s_1, \hat{s}_1) + L_1(s_2, \hat{s}_2). \quad (25)$$

**Tangent-space consistency loss  $\mathcal{L}_{tsc}$**  The tangent-space consistency loss aims to strengthen the constraints of multi-view polarization information on surface normal estimation. It ensures that the tangent plane consistency constraint is applied only when surface points are visible from the corresponding views. This is achieved through depth-guided visibility mask acquisition. It is defined as follows:

$$\mathcal{L}_{tsc} = \sum_{\mathbf{x}_s \in \mathcal{X}} \sum_{k \in K} \mathbf{V}(\mathbf{x}_s, k) \|\mathbf{T}_k(\mathbf{x}_s) \mathbf{n}(\mathbf{x}_s)\|_2^2, \quad (26)$$

where  $\mathcal{X}$  denotes the set of surface points, and  $K$  represents the number of neighboring views.

**Mask loss  $\mathcal{L}_m$**  The mask loss is used to make the rendering results of the object more accurate, which can be represented as:

$$\mathcal{L}_m = \Sigma \text{BCE}(\mathbf{M}, \hat{\mathbf{M}}). \quad (27)$$

**Opacity loss  $\mathcal{L}_o$**  The opacity loss follows Gaussian Surfels (Dai et al, 2024) to encourage the opacity of the Gaussian points to be close to 1 or 0. It can be represented as:

$$\mathcal{L}_o = \Sigma \exp(-20(o_i - 0.5)^2). \quad (28)$$

**Depth-normal consistency loss  $\mathcal{L}_d$**  The depth-normal consistency loss follows Gaussian Surfels (Dai et al, 2024) to make the rendered depth and normal of the object to be more consistent. It can be represented as:

$$\mathcal{L}_d = 1 - \tilde{\mathbf{N}} \cdot N(V(\tilde{\mathbf{D}})), \quad (29)$$

where  $V(\cdot)$  transforms each pixel and its depth to a 3D point and  $N(\cdot)$  calculates the normal from neighboring points using the cross product.

Table 2: Comparisons on synthetic dataset (SMVP3D (Han et al., 2024)) evaluated by mean angular error (MAE) ( $\downarrow$ ) with degree and Chamfer distance (CD) ( $\downarrow$ ) in millimeter (mm), respectively. Best and second results in SDF-based and 3DGS-based methods (except PolGS (Han et al., 2025)) are highlighted as 1st and 2nd. The time consumed is shown on the far right side of the table.

Method	HEDGEHOG		SQUIRREL		SNAIL		DAVID		Mean		time
	MAE	CD	MAE	CD	MAE	CD	MAE	CD	MAE	CD	
PANDORA (Dave et al., 2022)	9.41	9.50	10.85	5.88	8.08	10.97	14.75	4.88	10.77	7.81	10 h
NeRSP (Han et al., 2024)	8.94	6.57	8.23	3.02	5.56	3.72	15.38	4.18	9.53	4.37	10 h
MVAS (Cao et al., 2023)	4.30	4.22	6.10	3.73	3.30	7.87	8.47	3.21	5.54	4.76	11 h
GS-ROR (Zhu et al., 2025)	9.72	4.45	9.25	4.20	7.24	5.16	14.02	4.14	10.06	4.49	1.5 h
NeRO (Liu et al., 2023)	3.40	3.69	3.55	1.86	2.67	3.71	7.64	2.88	4.32	3.04	8 h
3DGS-DR (Ye et al., 2024)	12.28	12.66	17.18	11.20	11.42	20.70	20.56	7.91	15.36	13.12	12 min
Re-3DGS (Gao et al., 2024)	14.40	19.84	15.41	18.97	9.08	19.04	15.47	13.47	13.59	17.83	25 min
Gaussian Surfels (Dai et al., 2024)	16.50	8.82	21.65	9.53	19.05	14.04	21.56	7.39	19.69	9.95	5 min
PolGS++ (Ours)	8.33	6.99	9.18	6.08	7.25	9.20	13.36	5.12	9.53	6.85	10 min
PolGS (Han et al., 2025)	10.83	7.62	11.42	6.28	9.64	10.85	13.99	5.30	11.47	7.51	7 min

Table 3: Comparisons on real-world datasets (RMVP3D (Han et al., 2024) and PISR (Chen et al., 2024b)) evaluated by mean angular error (MAE) ( $\downarrow$ ) with degree and Chamfer distance (CD) ( $\downarrow$ ) in millimeter (mm), respectively. Best and second results in SDF-based and 3DGS-based methods (except PolGS (Han et al., 2025)) are highlighted as 1st and 2nd. The time consumed is shown on the far right side of the table.

Method	RMVP3D (Han et al., 2024)				PISR (Chen et al., 2024b)				Mean		time
	SHISA		FROG		L-RABBIT		S-RABBIT		MAE	CD	
	MAE	CD	MAE	CD	MAE	CD	MAE	CD			
PANDORA (Dave et al., 2022)	12.93	11.29	15.86	7.88	13.47	16.53	11.45	15.39	13.43	12.77	10 h
NeRSP (Han et al., 2024)	10.79	7.39	15.62	6.68	13.33	7.43	15.75	10.27	13.87	7.94	10 h
MVAS (Cao et al., 2023)	8.56	9.28	17.63	7.00	11.86	13.82	12.81	12.08	12.72	10.55	11 h
PISR (Chen et al., 2024b)	8.23	6.71	16.79	5.89	11.23	10.31	12.18	8.49	12.11	9.20	0.5 h
GS-ROR (Zhu et al., 2025)	12.50	5.30	14.68	5.97	18.82	16.40	21.55	19.87	16.89	11.89	1.5 h
NeRO (Liu et al., 2023)	8.41	4.88	15.29	5.39	9.40	7.81	8.34	6.30	10.36	6.10	8 h
3DGS-DR (Ye et al., 2024)	19.53	15.87	17.08	27.67	31.23	22.03	30.85	18.20	24.67	20.94	12 min
Re-3DGS (Gao et al., 2024)	16.69	14.66	17.85	13.35	29.19	15.66	26.39	20.20	22.53	15.97	25 min
Gaussian Surfels (Dai et al., 2024)	12.79	9.09	16.19	7.01	24.77	10.63	22.92	10.78	19.17	9.38	5 min
PolGS++ (Ours)	10.78	7.16	14.63	7.15	11.51	7.52	12.30	8.58	12.31	7.60	10 min
PolGS (Han et al., 2025)	10.88	7.76	15.03	7.48	11.55	7.76	12.73	9.29	12.55	8.07	7 min

## 5 Experiments

To evaluate the performance of our method, we conduct the following experiments: 1) Shape reconstruction on synthetic dataset, 2) Shape reconstruction on real-world dataset, 3) Ablation study and 4) Radiance decomposition.

**Dataset** We use four datasets to evaluate our method: the synthetic dataset SMVP3D (Han et al., 2024), the real-world dataset RMVP3D (Han et al., 2024), PANDORA (Dave et al., 2022) and PISR (Chen et al., 2024b), where PANDORA (Dave et al., 2022) can only be used for qualitative evaluation due to the lack of ground truth.

**Baselines** We compare our method with state-of-the-art techniques, including 3DGS methods Gaussian Surfels (Dai et al., 2024), 3DGS-DR (Ye et al., 2024), and Re-3DGS (Gao et al., 2024), and SDF-based methods NeRO (Liu et al., 2023), MVAS (Cao et al., 2023), PANDORA (Dave et al., 2022), NeRSP (Han et al., 2024), PISR (Chen et al., 2024b), and GS-ROR (Zhu et al., 2025) (which surface strongly depends

on SDF representation). All of these methods, except Gaussian Surfels (Dai et al., 2024), can handle reflective surfaces. MVAS (Cao et al., 2023), PANDORA (Dave et al., 2022), PISR (Chen et al., 2024b), and NeRSP (Han et al., 2024) utilize polarimetric information to reconstruct shapes. Specifically, we do not add the normal prior in Gaussian Surfels (Dai et al., 2024) among the whole experiments for fair comparisons.

**Evaluation metrics** We use the Chamfer Distance (CD) to evaluate the shape recovery performance and the mean angular error (MAE) to evaluate the quality of surface normal estimations. 3DGS-based methods provide point cloud results and we use Poisson surface reconstruction to generate the mesh for the evaluation.

**Implementation details** We conduct the experiments on an NVIDIA RTX 4090 GPU with 24GB memory. The training of our model is implemented in PyTorch 1.12.1 (Paszke et al., 2019) using the Adam optimizer Kingma and Ba (2014). The specific learning rates of different components in Gaussian kernels are set the same as Gaussian Surfels (Dai et al., 2024).

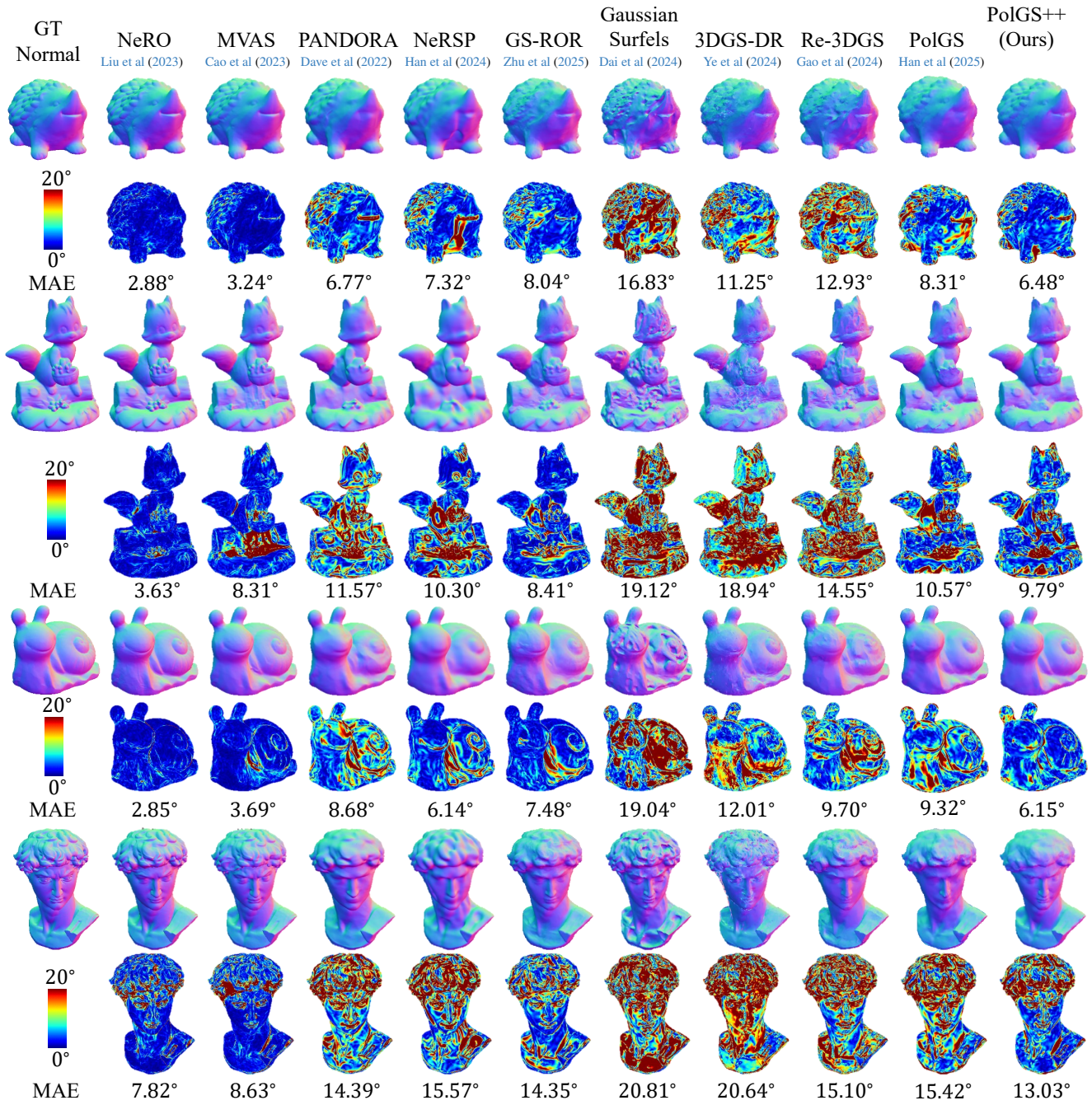


Fig. 6: Qualitative comparisons on surface normal in SMVP3D (Han et al, 2024), where our method can outperform existing methods based on the same representation and achieves comparable results with SDF-based methods.

We adopt a warm-up strategy to train the model, and we add the polarimetric information and deferred rendering after 1000 iterations.

### 5.1 Reconstruction results on synthetic dataset

In Fig. 6 and Table 2, we compare the shape recovery performance of various methods on the SMVP3D (Han et al, 2024), which contains four objects with spatially varying and reflec-

tive properties. However, it is worth noting that SDF-based methods, such as NeRO (Liu et al, 2023), GS-ROR (Zhu et al, 2025), MVAS (Cao et al, 2023), PANDORA (Dave et al, 2022), and NeRSP (Han et al, 2024), outperform 3DGS methods in terms of surface representation. This advantage is largely due to their superior ability to model complex surface details. Among the 3DGS methods, Gaussian Surfels (Dai et al, 2024) struggles with reflective surfaces, while 3DGS-DR (Ye et al, 2024) and Re-3DGS (Gao et al, 2024) still has

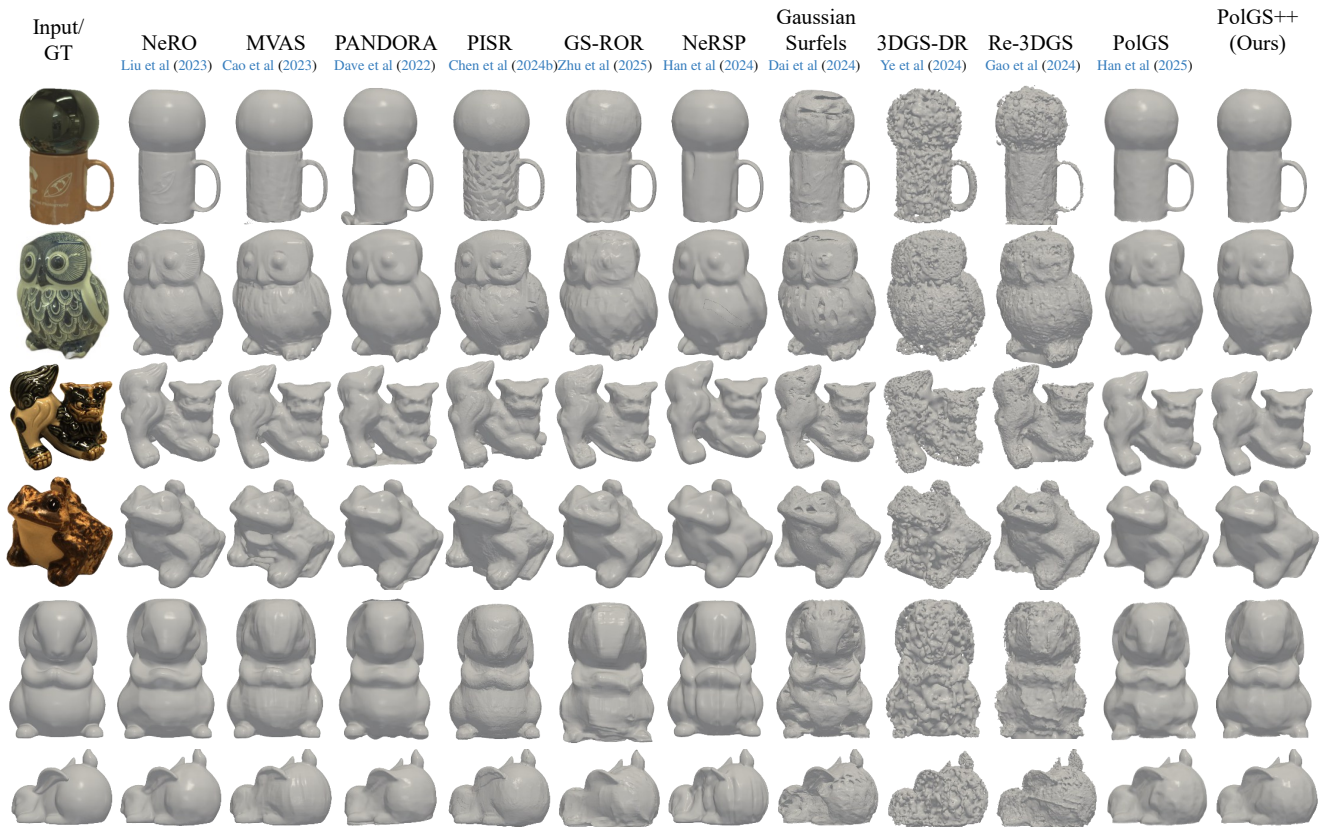


Fig. 7: Qualitative comparison shape on PANDORA (Dave et al, 2022), RMVP3D (Han et al, 2024) and PISR (Chen et al, 2024b), where PolGS produces similar quality of reconstruction mesh compared to SDF-based methods.

difficulty in representation of surface normal accurately. In contrast, PolGS++ effectively leverages polarimetric information, significantly improving geometric surface performance. Due to the inadequate point cloud generation by other 3DGS methods, they fail to produce reasonable mesh results using Poisson surface reconstruction. Our method, however, achieves the lowest mean Chamfer Distance across the synthetic SMVP3D (Han et al, 2024) dataset, reinforcing the trends observed in surface normal estimations and confirming that our approach delivers the best performance among the 3DGS techniques.

## 5.2 Reconstruction results on real-world dataset

We further evaluate the reconstruction performance on the PANDORA (Dave et al, 2022), RMVP3D (Han et al, 2024), and PISR (Chen et al, 2024b) datasets, with qualitative results illustrated in Fig. 7 and quantitative results detailed in Table 3. In real-world scenarios, our method produces reconstructions that align more closely with SDF-based approaches, while significantly outperforming other 3DGS-based methods in terms of reconstruction quality. For example, in the VASE case, our approach accurately estimates the shape of a ceramic surface in just 10 minutes, achieving results closer to

those generated by SDF-based methods. Additionally, the FROG sample highlights our method’s ability to reconstruct objects with rough glossy surfaces, showing the robustness and generalization capability of our method. Furthermore, texture-less object in PISR (Chen et al, 2024b) dataset also demonstrates the advantage of our method in handling objects with limited RGB cues, where the polarimetric information provides critical constraints for accurate shape recovery. These results collectively demonstrate the effectiveness of our approach in handling diverse real-world objects with varying surface properties.

## 5.3 Ablation study

In this section, we conduct two ablation studies to validate key design choices in our method.

**Effect of polarimetric information** We first study how polarimetric cues contribute to surface reconstruction. Our polarimetric supervision consists of two terms: a photometric polarization loss  $\mathcal{L}_{pol}$  and a tangent-space consistency loss  $\mathcal{L}_{tsc}$ . We perform controlled experiments on SMVP3D (Han et al, 2024) by varying both the number of input views and the enabled loss terms (w/o polarimetric loss, w/  $\mathcal{L}_{pol}$  only, and w/ both).

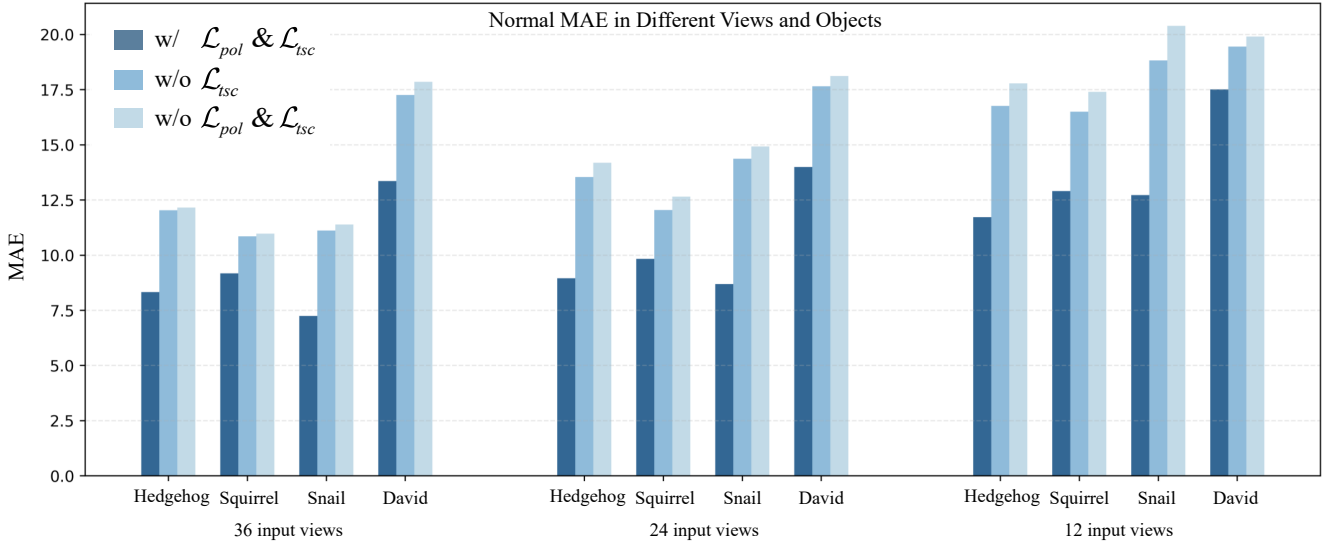


Fig. 8: Quantitative ablation results on SMVP3D (Han et al, 2024), where we evaluate the effect of polarimetric supervision under different input views.

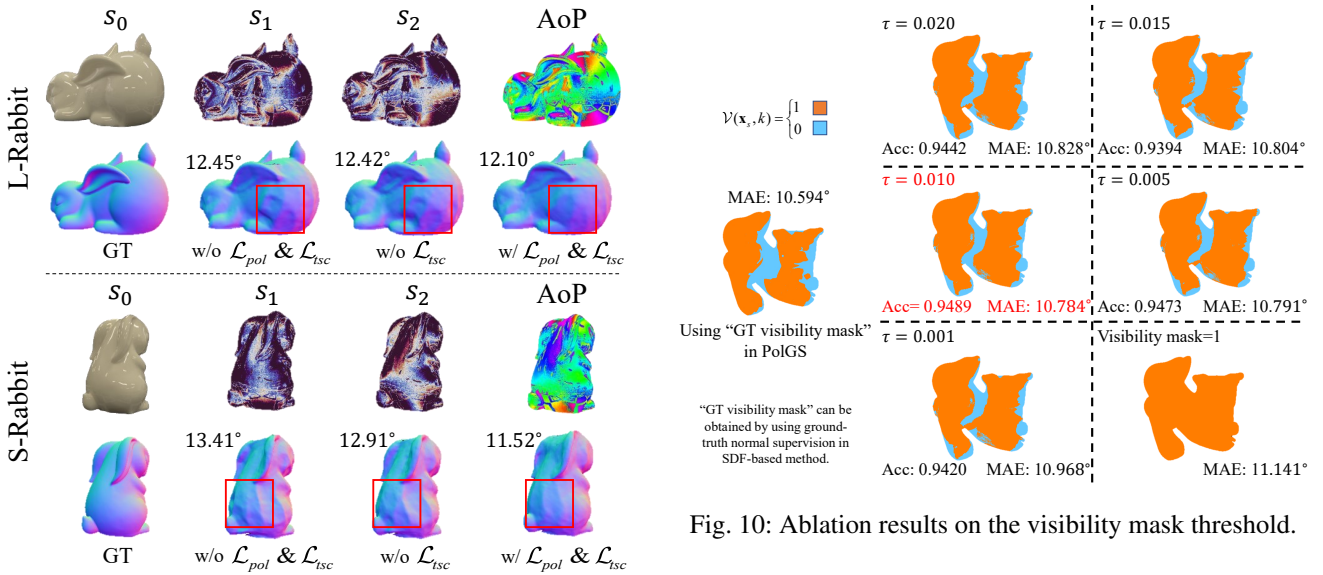


Fig. 9: Qualitative ablation results on PISR (Chen et al, 2024b), where we compare the reconstruction quality with and without polarimetric supervision.

Figure 8 shows a clear trend: when view coverage is dense, RGB photometric cues already provide strong constraints, and the additional gain from  $\mathcal{L}_{pol}$  becomes marginal. In contrast,  $\mathcal{L}_{tsc}$  yields a more consistent improvement, indicating that enforcing stable polarization-derived constraints is particularly beneficial even in well-observed settings. As the number of views decreases, the advantage of polarimetric information becomes increasingly evident, and combining  $\mathcal{L}_{pol}$  with  $\mathcal{L}_{tsc}$  leads to the most robust reconstructions under sparse-view conditions.

We further provide a qualitative evaluation on PISR (Chen et al, 2024b) to highlight the practical value of polarization in Fig. 9. While the RGB appearance lacks discernible texture, the polarization channels  $s_1$  and  $s_2$  and AoP information exhibit meaningful variations that provide additional geometric cues for resolving shape ambiguities. The results show that both concave and convex surface distortions are more accurately reconstructed when polarization information is employed.

**Visibility mask threshold** We then validate the threshold  $\tau$  used to binarize the depth-guided visibility mask in Equation (22). We sweep different thresholds and compare the resulting masks to the SDF-based visibility mask under ground-truth normal supervision.

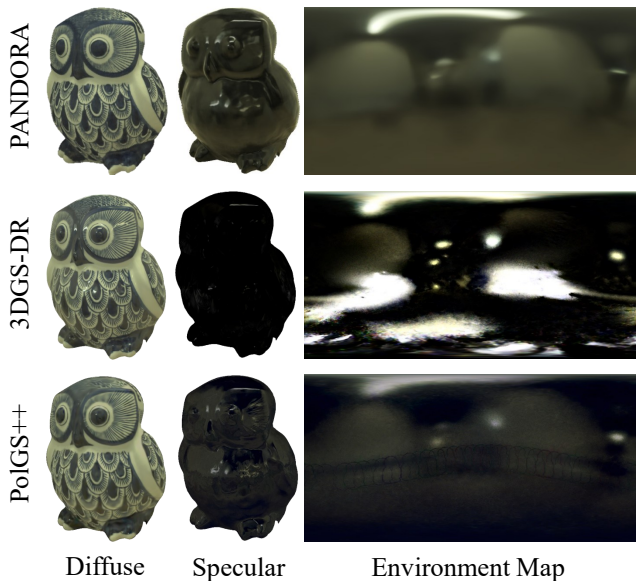


Fig. 11: Separation of diffuse and specular components with PANDORA (Dave et al, 2022), 3DGS-DR (Ye et al, 2024) and PoIGS++.

As shown in Fig. 10, directly using the SDF-based visibility masks yields a surface normal MAE of 10.594 degrees in PoIGS++. With depth-guided masks, performance varies with  $\tau$ , and  $\tau = 0.010$  provides the best trade-off: an accuracy of 0.9489 against the GT visibility mask and an MAE of 10.784 degrees. Without any visibility mask, the MAE degrades to 11.141 degrees, confirming the benefit of incorporating visibility information. We observe the same trend in other datasets and therefore use  $\tau = 0.010$  for all experiments in the paper.

#### 5.4 Comparison of radiance decomposition

Figure 11 presents a comparison of diffuse and specular component decomposition generated by PANDORA (Dave et al, 2022), 3DGS-DR (Ye et al, 2024), and PoIGS++. Here, PANDORA (Dave et al, 2022) utilizes the IDE Verbin et al (2022) structure to produce environment map results, whereas PoIGS++ adopts 3DGS-DR (Ye et al, 2024)’s methods by employing a Cubemap encoder for the same purpose. Compared with 3DGS-DR (Ye et al, 2024), PoIGS++ leverages additional polarimetric information to effectively constrain and disambiguate diffuse and specular components. Notably, our results closely align with PANDORA (Dave et al, 2022)’s, demonstrating improved radiance decomposition ability.

## 6 Conclusion

We propose PoIGS++, a physically-guided polarimetric Gaussian Splatting method for reflective surface reconstruction.

We leverage polarimetric cues to separate diffuse and specular components from the Stokes field, providing physically grounded constraints for surface normal estimation in the Gaussian Splatting representation. Furthermore, we introduce a depth-guided visibility mask acquisition method to enforce tangent-space consistency with AoP information, leading to improved reconstruction quality on reflective surfaces. Extensive experiments demonstrate that PoIGS++ outperforms state-of-the-art 3DGS-based methods in reconstruction accuracy while retaining high efficiency.

**Limitations** While PoIGS++ achieves strong results on reflective surfaces, it relies on accurate polarimetric measurements, which can be affected by noise and calibration errors. Moreover, PoIGS++ currently assumes a fixed environmental lighting condition and cannot handle dynamic lighting scenarios. Additionally, our method mainly focuses on dielectric materials. Future work could explore more robust polarimetric estimation techniques and extend the model to handle a wider range of materials and lighting conditions.

## References

- Ba Y, Gilbert A, Wang F, Yang J, Chen R, Wang Y, Yan L, Shi B, Kadambi A (2020) Deep shape from polarization. In: Proc. of European Conference on Computer Vision 3
- Baek SH, Jeon DS, Tong X, Kim MH (2018) Simultaneous acquisition of polarimetric SVBRDF and normals. *ACM Trans Graphic* 2, 3, 4, 5, 6
- Cao X, Santo H, Okura F, Matsushita Y (2023) Multi-View Azimuth Stereo via Tangent Space Consistency. In: Proc. of Computer Vision and Pattern Recognition 2, 3, 5, 7, 9, 10, 11
- Chen A, Xu Z, Geiger A, Yu J, Su H (2022) TensoRF: Tensorial radiance fields. In: Proc. of European Conference on Computer Vision 3
- Chen D, Li H, Ye W, Wang Y, Xie W, Zhai S, Wang N, Liu H, Bao H, Zhang G (2024a) Pgsr: Planar-based gaussian splatting for efficient and high-fidelity surface reconstruction. *IEEE Transactions on Visualization and Computer Graphics* 3
- Chen G, He Y, He L, Zhang H (2024b) PISR: Polarimetric neural implicit surface reconstruction for textureless and specular objects. In: Proc. of European Conference on Computer Vision 2, 3, 9, 11, 12
- Chen H, Li C, Lee GH (2023) NeuSG: Neural implicit surface reconstruction with 3d gaussian splatting guidance. *arXiv preprint arXiv:231200846* 2, 3
- Dai P, Xu J, Xie W, Liu X, Wang H, Xu W (2024) High-quality surface reconstruction using Gaussian Surfels. In: Proc. of ACM SIGGRAPH 2, 3, 4, 5, 6, 8, 9, 10, 11
- Dave A, Zhao Y, Veeraraghavan A (2022) PANDORA: Polarization-aided neural decomposition of radiance. In: Proc. of European Conference on Computer Vision 1, 2, 3, 4, 5, 8, 9, 10, 11, 13
- Deschaintre V, Lin Y, Ghosh A (2021) Deep polarization imaging for 3D shape and SVBRDF acquisition. In: Proc. of Computer Vision and Pattern Recognition 3
- Eftekhari A, Sax A, Malik J, Zamir A (2021) Omnidata: A scalable pipeline for making multi-task mid-level vision datasets from 3D scans. In: Proc. of Computer Vision and Pattern Recognition 6
- Gao J, Gu C, Lin Y, Li Z, Zhu H, Cao X, Zhang L, Yao Y (2024) Relightable 3D Gaussians: Realistic point cloud relighting with BRDF decomposition and ray tracing. In: Proc. of European Conference on Computer Vision 2, 3, 9, 10, 11
- Guédon A, Lepetit V (2024) SuGaR: Surface-aligned Gaussian Splatting for efficient 3D mesh reconstruction and high-quality mesh rendering. In: Proc. of Computer Vision and Pattern Recognition 2, 3
- Han Y, Guo H, Fukai K, Santo H, Shi B, Okura F, Ma Z, Jia Y (2024) NeRSP: Neural 3D Reconstruction for Reflective Objects with Sparse Polarized Images. In: Proc. of Computer Vision and Pattern Recognition 2, 3, 4, 5, 7, 9, 10, 11, 12
- Han Y, Tie B, Guo H, Lyu Y, Li S, Shi B, Jia Y, Ma Z (2025) PolGS: Polarimetric Gaussian Splatting for fast reflective surface reconstruction. In: Proc. of International Conference on Computer Vision 1, 2, 9, 10, 11
- Huang B, Yu Z, Chen A, Geiger A, Gao S (2024) 2D Gaussian Splatting for geometrically accurate radiance fields. In: Proc. of ACM SIGGRAPH 2, 3
- Kerbl B, Kopanas G, Leimkühler T, Drettakis G (2023) 3D Gaussian Splatting for real-time radiance field rendering. *ACM Trans Graphic* 2, 3, 4, 8
- Kingma DP, Ba J (2014) Adam: A method for stochastic optimization. *arXiv preprint arXiv:1412.6980* 9
- Lei C, Qi C, Xie J, Fan N, Koltun V, Chen Q (2022) Shape from polarization for complex scenes in the wild. In: Proc. of Computer Vision and Pattern Recognition 3
- Li C, Ngo TT, Nagahara H (2024a) Deep polarization cues for single-shot shape and subsurface scattering estimation. In: Proc. of European Conference on Computer Vision 3
- Li C, Ono T, Uemori T, Mihara H, Gatto A, Nagahara H, Moriuchi Y (2024b) NeISF: Neural Incident Stokes Field for Geometry and Material Estimation. In: Proc. of Computer Vision and Pattern Recognition 2, 3
- Li C, Ono T, Uemori T, Nitta S, Mihara H, Gatto A, Nagahara H, Moriuchi Y (2025) NeISF++: Neural incident stokes field for polarized inverse rendering of conductors and dielectrics. In: Proc. of Computer Vision and Pattern Recognition 2, 3
- Li J, Wang L, Zhang L, Wang B (2024c) TensoSDF: Roughness-aware tensorial representation for robust geometry and material reconstruction. *ACM Trans Graphic* 3
- Li R, Qiu S, Zang G, Heidrich W (2020) Reflection separation via multi-bounce polarization state tracing. In: Proc. of European Conference on Computer Vision 3
- Li Z, Jiang H, Cao M, Zheng Y (2023a) Polarized color image denoising. In: Proc. of Computer Vision and Pattern Recognition 3
- Li Z, Müller T, Evans A, Taylor RH, Unberath M, Liu MY, Lin CH (2023b) Neuralangelo: High-fidelity neural surface reconstruction. In: Proc. of Computer Vision and Pattern Recognition 3
- Liu Y, Wang P, Lin C, Long X, Wang J, Liu L, Komura T, Wang W (2023) NeRO: Neural geometry and BRDF reconstruction of reflective objects from multiview images. *ACM Trans Graphic* 1, 2, 3, 9, 10, 11
- Lyu X, Sun YT, Huang YH, Wu X, Yang Z, Chen Y, Pang J, Qi X (2024a) 3DGSr: Implicit surface reconstruction with 3D Gaussian Splatting. *ACM Trans Graphic* 2, 3
- Lyu Y, Cui Z, Li S, Pollefeys M, Shi B (2022) Physics-guided reflection separation from a pair of unpolarized and polarized images. *IEEE Transactions on Pattern Analysis and Machine Intelligence* 3
- Lyu Y, Zhao L, Li S, Shi B (2023) Shape from polarization with distant lighting estimation. *IEEE Transactions on Pattern Analysis and Machine Intelligence* 3
- Lyu Y, Guo H, Zhang K, Li S, Shi B (2024b) SfPUEL: Shape from polarization under unknown environment light. *Proc of Advances in Neural Information Processing Systems* 3
- Mildenhall B, Srinivasan PP, Tancik M, Barron JT, Ramamoorthi R, Ng R (2020) NeRF: Representing scenes as neural radiance fields for view synthesis. In: Proc. of European Conference on Computer Vision 2, 3
- Miyazaki, Tan, Hara, Ikeuchi (2003) Polarization-based inverse rendering from a single view. In: Proc. of International Conference on Computer Vision 3
- Müller T, Evans A, Schied C, Keller A (2022) Instant neural graphics primitives with a multiresolution hash encoding. *ACM Trans Graphic* 3
- Niemeyer M, Mescheder L, Oechsle M, Geiger A (2020) Differentiable volumetric rendering: Learning implicit 3D representations without 3D supervision. In: Proc. of Computer Vision and Pattern Recognition 3
- Oechsle M, Peng S, Geiger A (2021) UNISURF: Unifying neural implicit surfaces and radiance fields for multi-view reconstruction. In: Proc. of International Conference on Computer Vision 3
- Paszke A, Gross S, Massa F, Lerer A, Bradbury J, Chanan G, Killeen T, Lin Z, Gimelshein N, Antiga L, et al (2019) Pytorch: An imperative style, high-performance deep learning library. *Proc of Advances in Neural Information Processing Systems* 9
- Smith WA, Ramamoorthi R, Tozza S (2018) Height-from-polarisation with unknown lighting or albedo. *IEEE Transactions on Pattern Analysis and Machine Intelligence* 3
- Verbin D, Hedman P, Mildenhall B, Zickler T, Barron JT, Srinivasan PP (2022) Ref-NeRF: Structured view-dependent appearance for neural radiance fields. In: Proc. of Computer Vision and Pattern Recognition 2, 3, 13
- Walter B, Marschner SR, Li H, Torrance KE (2007) Microfacet models for refraction through rough surfaces. In: Proceedings of the 18th Eurographics conference on Rendering Techniques 5
- Wang H, Hu W, Zhu L, Lau RW (2024) Inverse rendering of glossy objects via the neural plenoptic function and radiance fields. In: Proc.

- of Computer Vision and Pattern Recognition 3
- Wang P, Liu L, Liu Y, Theobalt C, Komura T, Wang W (2021) NeuS: Learning neural implicit surfaces by volume rendering for multi-view reconstruction. arXiv preprint arXiv:210610689 3, 5, 6
- Wang X, Zhang Y, Chen Y (2025) Polarized reflection removal with dual-stream attention guidance. Pattern Recognition 3
- Wang Y, Skorokhodov I, Wonka P (2022) Hf-NeuS: Improved surface reconstruction using high-frequency details. Proc of Advances in Neural Information Processing Systems 3
- Wang Y, Han Q, Habermann M, Daniilidis K, Theobalt C, Liu L (2023) NeuS2: Fast learning of neural implicit surfaces for multi-view reconstruction. In: Proc. of International Conference on Computer Vision 3
- Yang L, Ruizheng W, Jiyong L, Ying-cong C (2024) GNeRP: Gaussian-guided neural reconstruction of reflective objects with noisy polarization priors. arXiv preprint arXiv:240311899 3
- Yariv L, Kasten Y, Moran D, Galun M, Atzmon M, Ronen B, Lipman Y (2020) Multiview neural surface reconstruction by disentangling geometry and appearance. Proc of Advances in Neural Information Processing Systems 3
- Yariv L, Gu J, Kasten Y, Lipman Y (2021) Volume rendering of neural implicit surfaces. Proc of Advances in Neural Information Processing Systems 3
- Ye K, Hou Q, Zhou K (2024) 3D Gaussian Splatting with deferred reflection. In: ACM SIGGRAPH 2, 3, 7, 9, 10, 11, 13
- Yu M, Lu T, Xu L, Jiang L, Xiangli Y, Dai B (2024a) GSDF: 3DGS meets SDF for improved neural rendering and reconstruction. Proc of Advances in Neural Information Processing Systems 2, 3
- Yu Z, Sattler T, Geiger A (2024b) Gaussian opacity fields: Efficient adaptive surface reconstruction in unbounded scenes. ACM Trans Graphic 3
- Zhao J, Monno Y, Okutomi M (2022) Polarimetric multi-view inverse rendering. IEEE Transactions on Pattern Analysis and Machine Intelligence 2, 3
- Zhou C, Han Y, Teng M, Han J, Li S, Xu C, Shi B (2023) Polarization guided HDR reconstruction via pixel-wise depolarization. IEEE Transactions on Image Processing 3
- Zhu Z, Wang B, Yang J (2025) GS-ROR2: Bidirectional-guided 3DGS and SDF for reflective object relighting and reconstruction. ACM Trans Graphic 2, 3, 9, 10, 11
- Zwicker M, Pfister H, Van Baar J, Gross M (2001) Surface splatting. In: Proceedings of the 28th annual conference on Computer graphics and interactive techniques 4
- Zwicker M, Pfister H, Van Baar J, Gross M (2002) Ewa splatting. IEEE Transactions on Visualization and Computer Graphics 4